Don't mind the gap: reframing the Perren strain rule for fracture healing using insights from virtual mechanical testing

From Lehigh University, Bethlehem, Pennsylvania, USA

M. Tanveer,[1] K. Klein,[2] B. von Rechenberg,[2,3] S. Darwiche,[2] H. L. Dailey[1]

[1]Department of Mechanical Engineering & Mechanics, Lehigh University, Bethlehem, Pennsylvania, USA
[2]Musculoskeletal Research Unit (MSRU), Vetsuisse Faculty, University of Zurich, Zurich, Switzerland
[3]Competence Center of Applied Biotechnology and Molecular Medicine (CABMM), Vetsuisse Faculty, University of Zurich, Zurich, Switzerland

Correspondence should be sent to Hannah L. Dailey
hlr3@lehigh.edu

Aims

The "2 to 10% strain rule" for fracture healing has been widely interpreted to mean that interfragmentary strain greater than 10% predisposes a fracture to nonunion. This interpretation focuses on the gap-closing strain (axial micromotion divided by gap size), ignoring the region around the gap where osteogenesis typically initiates. The aim of this study was to measure gap-closing and 3D interfragmentary strains in plated ovine osteotomies and associate local strain conditions with callus mineralization.

Methods

MicroCT scans of eight female sheep with plated mid-shaft tibial osteotomies were used to create image-based finite element models. Virtual mechanical testing was used to compute postoperative gap-closing and 3D continuum strains representing compression (volumetric strain) and shear deformation (distortional strain). Callus mineralization was measured in zones in and around the osteotomy gap.

Results

Gap-closing strains averaged 51% (mean) at the far cortex. Peak compressive volumetric strain averaged 32% and only a small tissue volume (average 0.3 cm^3) within the gap experienced compressive strains > 10%. Distortional strains were much higher and more widespread, peaking at a mean of 115%, with a mean of 3.3 cm^3 of tissue in and around the osteotomy experiencing distortional strains > 10%. Callus mineralization initiated outside the high-strain gap and was significantly lower within the fracture gap compared to around it at nine weeks.

Conclusion

Ovine osteotomies can heal with high gap strains (> 10%) dominated by shear conditions. High gap strain appears to be a transient local limiter of osteogenesis, not a global inhibitor of secondary fracture repair.

Article focus

- The famous "2 to 10% strain rule" considers a highly simplified mechanical approximation of the effects of interfragmentary motion as the global limiter of fracture healing.
- The purpose of this study was to use computational modelling and image data analysis to assess the local relationship between 3D strain (granulation tissue deformation) and later mineralization of the callus.

Key messages

- High strain conditions exist in and around the fracture gap, greatly exceeding 10% strain and dominated by shear deformation.
- Callus mineralization is initiated outside the high-strain fracture gap where

conditions for bone formation are more favourable.
- Fracture gap-closing strains above 10% do not cause nonunion.

Strengths and limitations
- High-fidelity computational modelling allows non-invasive measurement of the true 3D strain environment, considering both inside the fracture gap and the perifragmentary region around it, where new bone forms first.
- Study limitations include the use of only one surgical model (plate type and osteotomy size) and lack of longitudinal imaging data. The absolute limiting condition for strain and bone healing remains unknown.

Introduction
Bone repair is fundamentally a mechanoregulated process.[1] Interfragmentary motion produces strain (deformation) of the interfragmentary tissues and this induces secondary healing by callus formation. During secondary healing, bone integrity is gradually restored by the formation of fibrous tissue, cartilaginous tissue, and finally woven and lamellar bone by endochondral ossification.[2,3] Intramembranous bone formation also occurs via the differentiation of mesenchymal progenitor cells into osteoblasts. Progressive mineralization stiffens the callus and reduces interfragmentary motion over time.[4] Over the last 40 years, numerous large animal and clinical studies have shown that fracture healing is highly responsive to implant-mediated changes in the mechanical conditions at the fracture site.[5-14]

Research interest in the role of mechanical factors in the augmentation or inhibition of fracture repair traces its roots to the seminal work of Prof Stephan Perren.[15,16] Perren recognized that mechanical stimulation is a central driver of fracture repair, and focused on the gap-closing strain – the amount of axial motion across the fracture gap divided by the gap size. Perren drew logical deductions from elongation rupture testing of cartilage and cortical bone to hypothesize strain tolerance limits for successful bone healing. The resulting "2 to 10% strain rule" has since been widely interpreted to mean that a gap-closing strain below 2% does not provide enough stimulation for callus formation, while gap strain above 10% hinders osteogenesis and increases the risk of nonunion.

This modern oversimplification of Perren's strain theory has crystallized into dogma, appearing in textbooks,[17,18] numerous publications, and websites and YouTube videos with millions of views.[19-21] Despite its ubiquity, the 2 to 10% rule is directly contradicted by decades of evidence from in vivo studies in large animals and humans. For example, ovine osteotomies heal well with axial gap closing strains of 31% to 36%.[22,23] Human tibial fractures fixed with axial micromotion (gap-closing strains 20% to 33%) heal more quickly than with rigid fixation.[13,24] Hente and Perren (posthumous)[25] used a wedge osteotomy to create interfragmentary strain gradients and demonstrated callus formation with gap strains up to 24%. Plated distal femur fractures likely experience interfragmentary strains well above 50% without causing nonunion.[26] Perren[27] theorized that fractures can tolerate initial high strains because the first repair tissues are highly compliant, gradually stiffening in a 3D matrix of callus to bring strain levels within tolerable limits for later bone formation.

These studies and others suggest that fracture healing is likely much more tolerant to strain than the simple interpretation of the 2 to 10% rule suggests. However, revisiting the Perren strain theory is challenging because 3D tissue strains cannot be directly measured in vivo, and the concept of "gap strain" neglects the periosteal region around the fracture where callus mineralization typically initiates. Accordingly, the objective of this study was to deploy virtual mechanical testing together with image data-mining techniques to probe the early interfragmentary strain environment and measure callus mineralization in a well-established ovine osteotomy model. To achieve this, we used finite element analysis (FEA) to compute interfragmentary motions under physiological loading and translate those motions to tissue-level continuum strains. The hypothesis of this study was that high initial interfragmentary gap strains (> 10%) exist in this surgical model and are associated with a local delay in mineralization, but not nonunion.

Methods
Animal specimens and scan information
Eight female Swiss Alpine sheep (average body weight 68 kg, age 2 to 3 years) with mid-shaft tibial osteotomies were used for this analysis. The operated limb had a 3 mm gap osteotomy stabilized with a medial 12-hole stainless steel plate (broad straight veterinary 3.5 mm locking compression plate (LCP), 159 mm in length, with 3.5 mm bicortical screws; DePuy Synthes). A 3 mm defect in sheep is a non-critical defect capable of spontaneous healing. Animals were maintained for nine weeks after surgery and kept in individual stalls (approximately 2 m^2) with hard floors bedded with straw. They received a full cast up over the stifle joint, which allowed them to put weight on the limb immediately after surgery, but hindered them in bending their limbs. Within their individual stalls, sheep were allowed to roam freely. Clinical checks for health status (including lameness/weightbearing) were performed twice a day throughout the postoperative period, and peri- and postoperative analgesia and antibiosis were continued for four days after surgery. More details regarding the animal study are described in a previously published study.[28]

After kill, the tibiae were excised, stripped of soft-tissue keeping the periosteum intact, and the plate and screws were removed from the operated limb, taking care not to disrupt the callus region. Samples were wrapped in saline-soaked gauze to maintain hydration. Postmortem microCT scans of the diaphyseal segments were performed using an XtremeCT II Micro-CT scanner (Scanco Medical AG, Switzerland) with voltage 68 kVp and current 1,470 µA. The resulting isotropic scan resolution was 60.7 µm. A phantom (Scanco KP70 phantom, QRM) calibration scan was performed to allow conversion of voxel data for CT attenuation (Hounsfield units (HU)) to bone mineral density (BMD, ρ^{QCT} (mgHA/cm^3)). Radiological union scoring was performed by two independent, board-certified expert reviewers (BvR, MF, see Acknowledgements) to evaluate the presence or absence of nonunion using a published scoring system.[29] These animals were randomly selected from a previously completed research study, and the data reuse for this new analysis is consistent
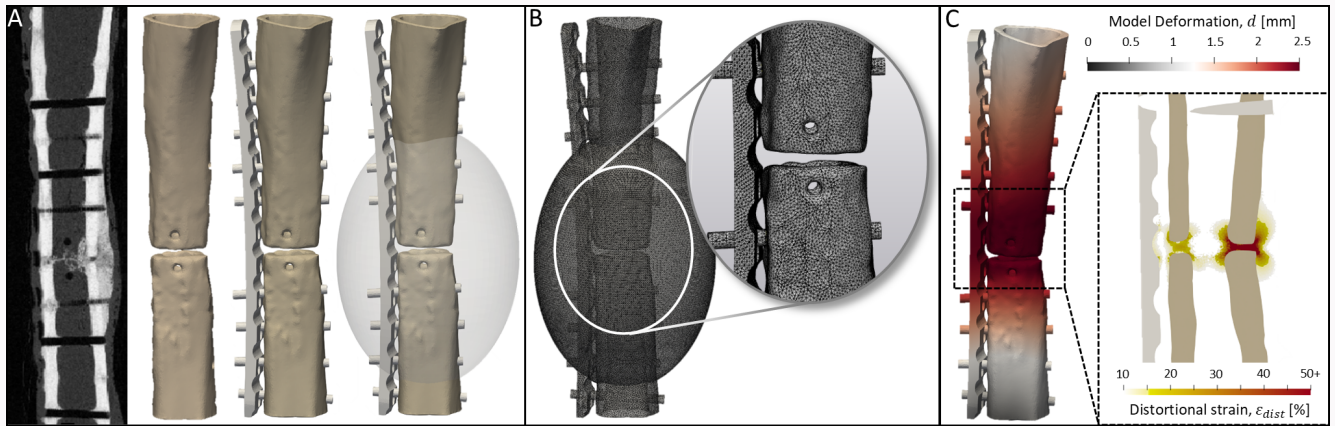
Fig. 1

a) Operated tibia models were created from the microCT scans at nine weeks, and the implants were implanted virtually. b) Bone and implant models were meshed with a negligible-stiffness sub-model around the fracture gap zone to visualize strain in this region. c) Calculated deformations from the bone and implant models were used as displacement boundary conditions in the strain visualization sub-models, producing calculated strain values for the entire perifragmentary region (inset).

with the 3Rs principles.[30] All experiments were conducted according to the Swiss laws of animal protection and welfare, and the protocol was authorized by the local governmental veterinary authorities. The study adhered to the ARRIVE guidelines and the checklist has been supplied as Supplementary Material.

Scan processing and finite element model creation

To prepare the image-based finite element (FE) models, scans were processed in Mimics (v23.0; Materialise, Belgium). Scans were down-sampled to an isotropic resolution of 400 μm, comparable to clinical resolution. Operated bones were initially segmented using a radiodensity range of 2,500 to 4,000 HU to preliminarily isolate old cortical bone from callus based on a previously validated segmentation process performed on the same dataset.[29] The choice of thresholds was specific to the dataset and will vary based on the scan settings. Cortical bone geometry reconstruction was performed by manually correcting the mask boundaries around the osteotomy in the regions where remodelling had made the cortical bone less dense.[31,32] The immediate postoperative radiographs and bone structure above the osteotomy were used as a guide to reconstruct preoperative bone shapes without cortical remodelling. These operations were performed using masking, contouring, and surface optimization tools in Mimics. All reconstructions were reviewed by the senior author (HLD). No callus was included for these models. Medullary void spaces were excluded.

Finite element models representing the postoperative (unhealed) conditions were created following the procedure shown in Figure 1. Virtual plate installation was performed in Solidworks 2020 (Dassault Systèmes, France). The plate and screw locations were specimen-specific and were matched to the corresponding screw holes in each osteotomized tibia scan. Screws were modelled without the screw threads, a valid simplification to reduce computational cost when the global load-deformation behaviour, not screw-bone interaction (e.g. pullout force), is the primary outcome measure.[33,34] A 3D interfragmentary strain visualization region was added to measure strains within and around the fracture gaps of the

operated tibiae. Contact conditions between bone and screws were defined as bonded, and frictionless contact was defined between plate and bone and between the bone fragments.[26]

FE meshes were created using 3-Matic (v15.0; Materialise), utilizing quadratic tetrahedral elements (tet-10) with a maximum edge length of 1 mm. A non-manifold assembly was created for the operated bone model including the strain visualization region and the hardware. Elementwise material properties were applied in the bone region using a validated scaling equation for ovine tibial cortical bone:

$$E = 10225 \, \rho_{QCT} \tag{1}$$

where the Young's modulus E is in MPa. Poisson's ratio was $v = 0.3$.[29] A homogeneous soft material with $E = 0.5$ MPa and $v = 0.45$ was assigned to the strain visualization region. Material properties of stainless steel was applied to the plate and screws with $E = 183.6$ GPa and $v = 0.35$.[35]

Boundary conditions and loading

FE analysis was performed in ANSYS Workbench Mechanical (R2020; ANSYS, USA). Boundary conditions were defined based on a recent biomechanical study that examined plate bending under ex vivo loading conditions similar to physiological conditions.[35] Remote points were established at the proximal and distal faces of the cortical bone segments with offsets of 50 mm and 10 mm, respectively, representing the tibiofemoral and tibiotarsal joints. The coordinate systems of the remote points were aligned along the mechanical axis of the bone. A roller support was defined on the proximal remote point to allow translation of bone along the vertical axis (z) with rotation about the x- and y-axes. A pinned support was defined on the distal remote point to represent the rotation of bone about the tibiotarsal joint during loading, while restricting translation in all directions.

No gait analysis data were available for the animals in the previously completed preclinical study, so tibial loading had to be estimated using literature data. We applied a representative instantaneous axial load of 600 N (0.9 BW) based on a previous report of early (one week) postoperative loading through an instrumented external fixator in a similar

Don't mind the gap: reframing the Perren strain rule for fracture healing using insights from virtual mechanical testing
M. Tanveer, K. Klein, B. von Rechenberg, S. Darwiche, H. L. Dailey

7
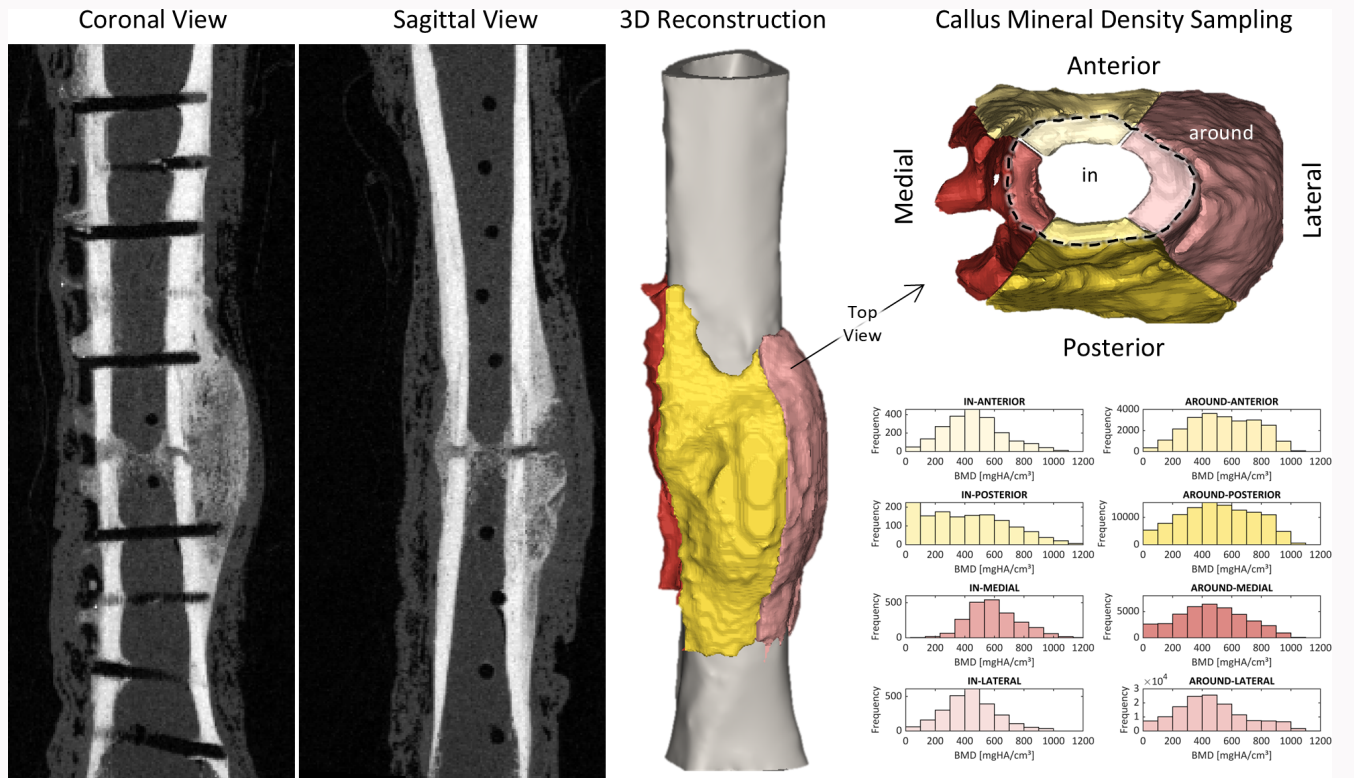
Fig. 2
Representative CT scan slice views and 3D reconstruction with callus masking by zone (within or around the fracture gap) and quadrant (anterior, posterior, medial, and lateral). Callus mineral density was sampled for voxels in each of the eight regions of interest.

animal model (tibial osteotomy in adult female sheep).[36] To prevent the strain visualization region from influencing bone movements, sub-modelling was performed in ANSYS as a two-step process. Calculated displacements of the bone fragments and implant components were carried forward as displacement boundary conditions in the sub-models for calculation of perifragmentary continuum strains (Figure 1c).

Voxel data sampling and mapping
To examine the relationship between strain and mineralization within the callus, BMD (ρQCT) was sampled for voxels located within and around the fracture gap. Each callus was subdivided into eight segments: two zones ('in' for the interfragmentary gap, and 'around' for the periosteal region) and four quadrants ('medial', 'lateral', 'anterior', and 'posterior'). The resulting callus segments with associated BMD data are illustrated in Figure 2. Voxel data for each sampling region were also mapped to two continuum strain invariants calculated in the strain visualization region – volumetric strain (ε_{vol}) representing volumetric compression or dilation, and distortional strain (ε_{dist}) representing shear or shape change:

$$\varepsilon_{Vol} = \varepsilon_1 + \varepsilon_2 + \varepsilon_3 \qquad (2)$$

$$\varepsilon_{Dist} = \frac{\sqrt{2}}{2}((\varepsilon_1 - \varepsilon_2)^2 + (\varepsilon_1 - \varepsilon_3)^2 + (\varepsilon_2 - \varepsilon_3)^2)^{\frac{1}{2}} \qquad (3)$$

These two scalar strain quantities from the 3D general state of strain were selected because they have been previously identified as drivers of tissue differentiation in computational mechanoregulation models of fracture

healing.[37] Between the bone ends, a gap-closing (Perren) strain was calculated by measuring gap-closing distance, and dividing that by the original distance between the selected nodes.

Statistical analysis
Post-processing of simulation results was performed in MATLAB (R2022; MathWorks, USA). Statistical analysis was run in SPSS Statistics (29.0; IBM, USA). For each of the eight callus segments in each model, the callus volume (cm³) and median BMD (mgHA/cm³) were reported. The general linear model (GLM) repeated-measures procedure (one-way and two-way ANOVA) was run in SPSS for callus BMD and volume with the following within-subjects factors: zone and quadrant. All pairwise comparisons included Bonferroni adjustments for multiple comparisons. Linear regression was also run to predict BMD based on zone, quadrant, and strain. Data are reported as mean (SD) following confirmation of normality in each test. A p-value < 0.05 was considered statistically significant.

Results
This medially plated osteotomy fracture model induced formation of a lateral-dominant bridging callus. The radiological progression of callus showed the classic pattern of callus volumetric growth, progressive mineralization predominantly outside the osteotomy, followed by infilling of the osteotomy over time (Figure 3).
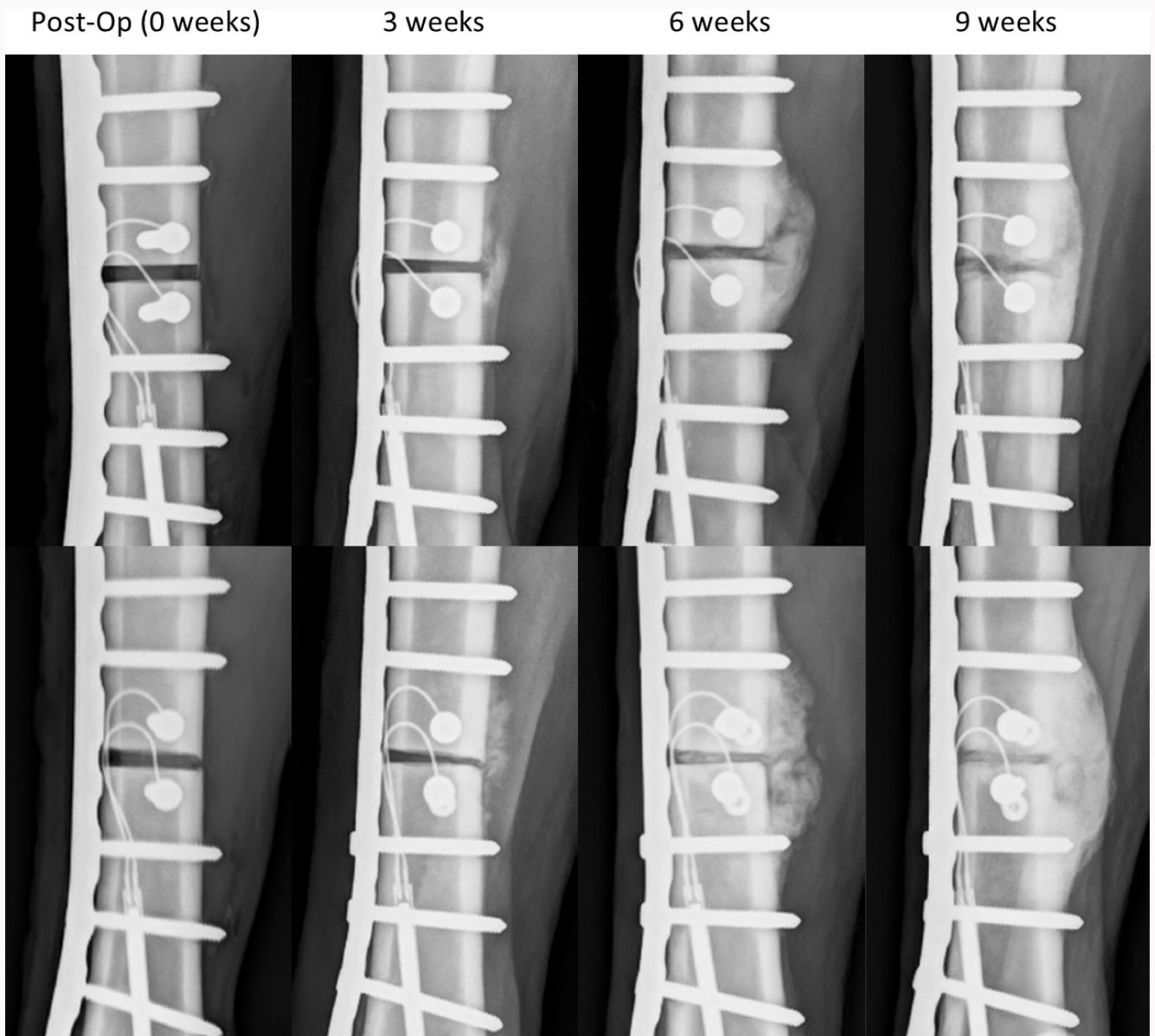
Fig. 3
Anteroposterior radiographs of two representative animals taken immediately postoperatively and at three, six, and nine weeks. Callus formation was laterally dominant in this medial plating model.

Interfragmentary motion and peak strains

To illustrate the associations between interfragmentary motion and strain, representative results are presented for one animal in Figure 4 and summary results for all animals in Figure 5. Peak interfragmentary motions occurred at the far cortex (mean lateral gap closure 1.32 mm (SD 0.160)). These interfragmentary motions were associated with gradients of Perren (gap-closing) strains within the gap zone. Mean gap-closing strains varied from 8.49% (SD 1.55%) at the near cortex to 51.1% (SD 10.2%) at the far cortex. The two continuum strain invariants ε_{vol} and ε_{dist} also had strong gradients in and around the fracture gap, with the highest strains occurring at the far cortex. Mean volumetric strain was predominantly compressive, peaking at -32.0% (SD 10.4%) at the far cortex. Mean distortional strains were also high, peaking at 115% (SD 16.9%) at the far cortex. The mean total volume of elements with distortional strains greater than 10% was 3.3 cm³ (SD

0.70), and the total volume of elements with absolute value compressive volumetric strains greater than 10% was 0.30 cm³ (SD 0.20). The mean callus volume experiencing initial distortional strain > 10% corresponded to 40% (SD 29%) of the nine-week final callus volume. The mean callus volume experiencing initial volumetric strain > 10% was much smaller, only 3.9% (SD 5.1%) of the nine-week final callus volume.

Spatial distribution of callus volume, density, and strain

Callus volume and BMD as well as peak distortional and volumetric strains were calculated for each callus zone and quadrant (Figure 6). Statistical results are presented in brief, with complete analysis including tests of assumptions provided in the Supplementary Material.

Callus volume was only reported for the 'around' zone and was largest in the 'lateral' and 'posterior' quadrants. Across the different 'around' zones, callus volume was significantly

Don't mind the gap: reframing the Perren strain rule for fracture healing using insights from virtual mechanical testing
M. Tanveer, K. Klein, B. von Rechenberg, S. Darwiche, H. L. Dailey

9
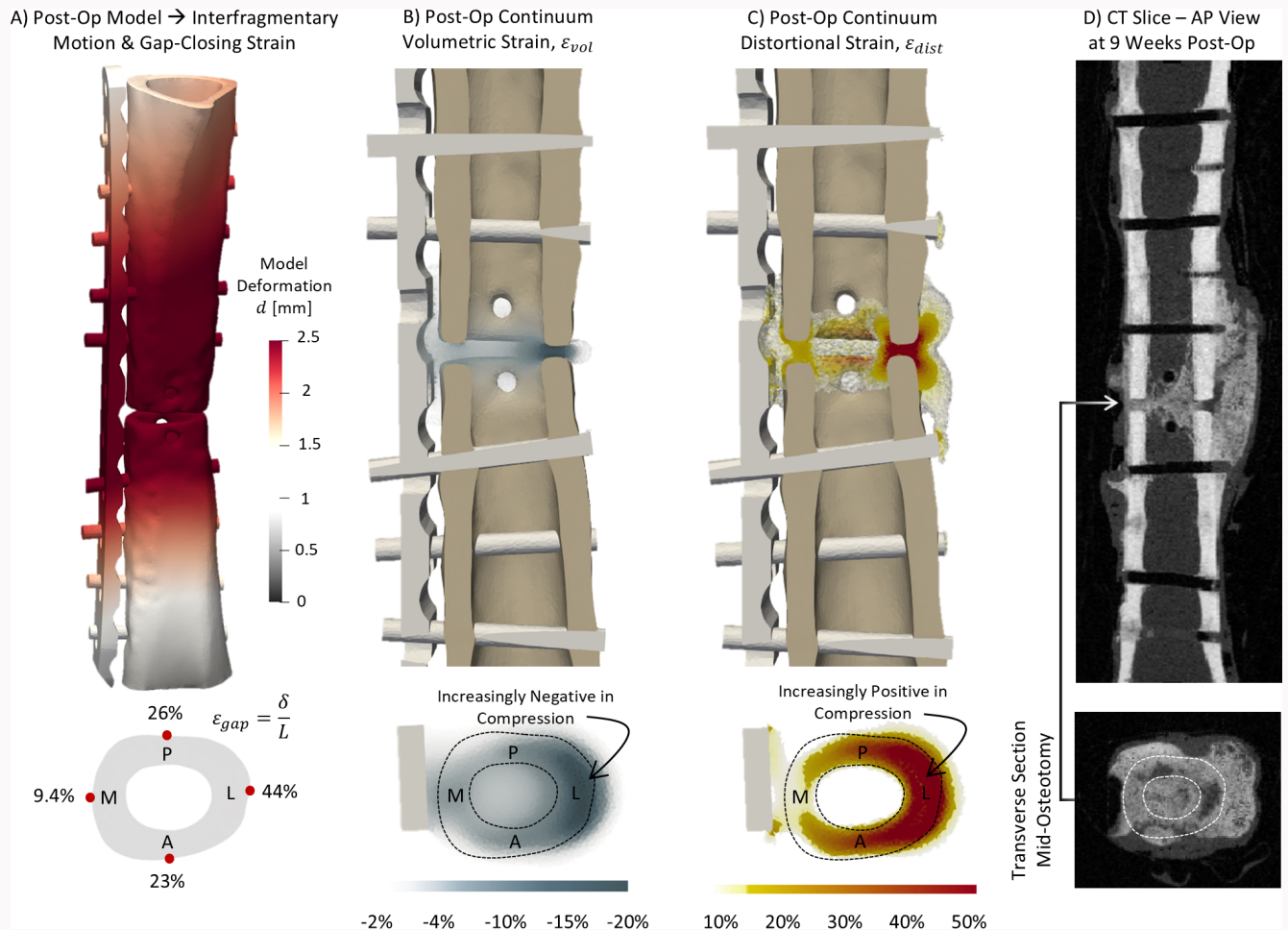
Fig. 4

a) Representative postoperative (unhealed) model showing highest gap-closing strains at the far cortex due to plate bending. Continuum strains calculated in the perifragmentary zone show concentrations of compressive b) volumetric strain and c) distortional strain immediately within and around the fracture gap. d) Post-mortem microCT at nine weeks shows a successfully bridged callus with pockets of delayed mineralization at the fracture line.
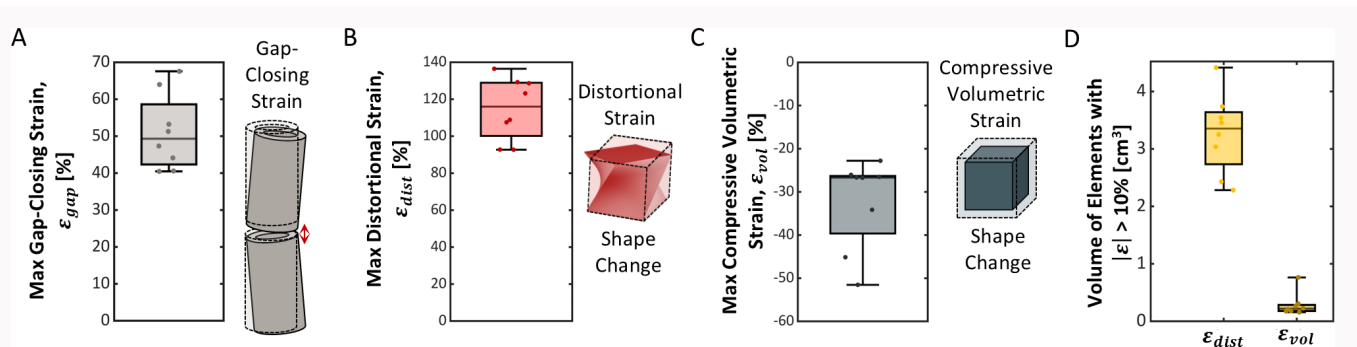
Fig. 5

Postoperative (unhealed) strain results for all animals: a) maximum gap-closing strain, b) maximum distortional strain (ε_{dist}), c) maximum compressive volumetric strain (ε_{vol}), and d) volume of elements with strains greater than 10% distortional or 10% absolute value volumetric.

different (p < 0.001). Bonferroni-adjusted pairwise comparisons showed mean medial callus volume (1.12 cm³ (SD 0.869)) and mean anterior callus volume (0.977 cm³ (SD 0.694)) as not significantly different from each other. However, both zones were significantly different from mean lateral callus volume (4.82 cm³ (SD 3.16)) and mean posterior callus volume (3.98 cm³ (SD 2.34)) (all p < 0.05).

A higher median BMD was observed in the 'around' zone compared to 'in' for quadrants 'lateral', 'anterior', and 'posterior'. For the 'around' zone, BMD was statistically different based on quadrant (two-way ANOVA, simple main effects; p < 0.001). Bonferroni-adjusted pairwise comparisons were statistically significant for BMD in the following segment pairings: 'around'-'medial' versus 'around'-'posterior' (p =
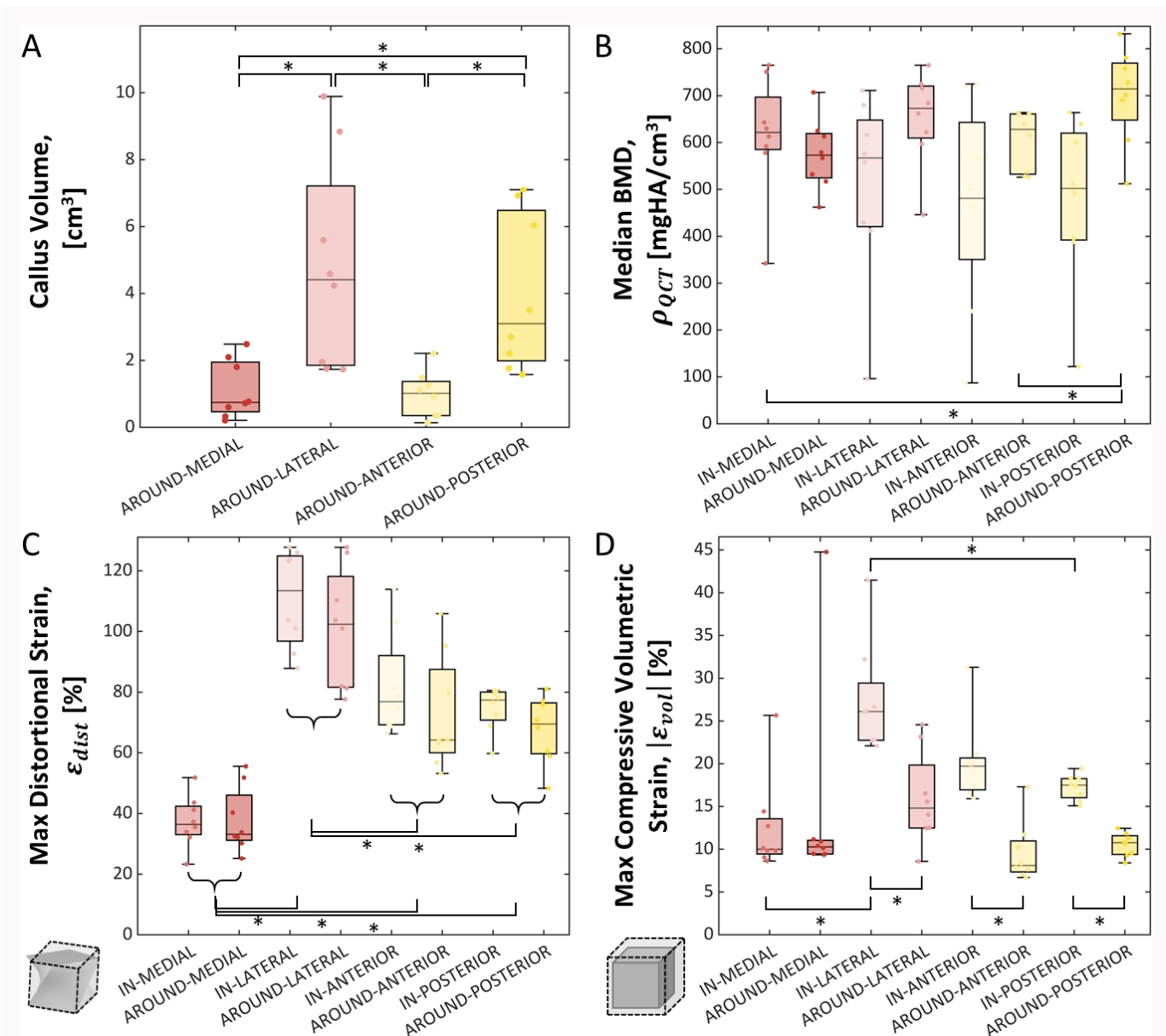
Fig. 6
Strain and mineralization metrics by zone and quadrant for all animals: a) callus volume, b) median bone mineral density (BMD), c) distortional strain, and d) volumetric strain. Strains tended to be higher in the gap compared to around, and BMD tended to be lower.

0.003), and 'around'-'anterior' versus 'around'-'posterior' (p = 0.032).

As expected with plate bending leading to far-cortical gap closure, the highest distortional strains were observed in the 'lateral' region, while the lowest strains were in the 'medial' region. In the two-way ANOVA, there was no statistically significant two-way interaction between zone and quadrant for distortional strain. The simple main effect of zone showed that there was a statistically significant difference in distortional strain between the 'in' and 'around' locations, $F_{(1,7)}$ = 9.77 (p = 0.017). The simple main effect of quadrant showed a statistically significant difference in distortional strain across the four locations, $F_{(3,21)}$ = 43.7 (p < 0.001). Bonferroni-adjusted pairwise comparisons were significant (Figure 6c, all p ≤ 0.013) for all quadrant pairings except for between 'anterior' and 'posterior' (p > 0.999).

The highest absolute value volumetric strains were observed in the 'lateral' region, with the gap zone ('in')

experiencing greater compression compared to 'around'. There was a statistically significant two-way interaction between zone and quadrant, $F_{(3,21)}$ = 8.98 (p < 0.001, two-way ANOVA). Simple main effects of zone were checked for each quadrant, and of quadrant for each zone. These comparisons confirmed multiple statistically significant differences in volumetric strains with location (Figure 6d, all p ≤ 0.001, two-way ANOVA, simple main effects; see Supplementary Material for full details).

Discussion

The results of this study agree with other ovine osteotomy studies that have documented successful fracture healing with initial axial gap-closing strains above 30%.[22,23] In human tibial fractures, micromotion in the 1 mm range (estimated gap-closing strain 30% to 50% for an ideal 2 to 3 mm fracture gap after anatomical reduction) has been shown to accelerate secondary healing.[13,24,38] In all our models, the peak

Don't mind the gap: reframing the Perren strain rule for fracture healing using insights from virtual mechanical testing
M. Tanveer, K. Klein, B. von Rechenberg, S. Darwiche, H. L. Dailey

11
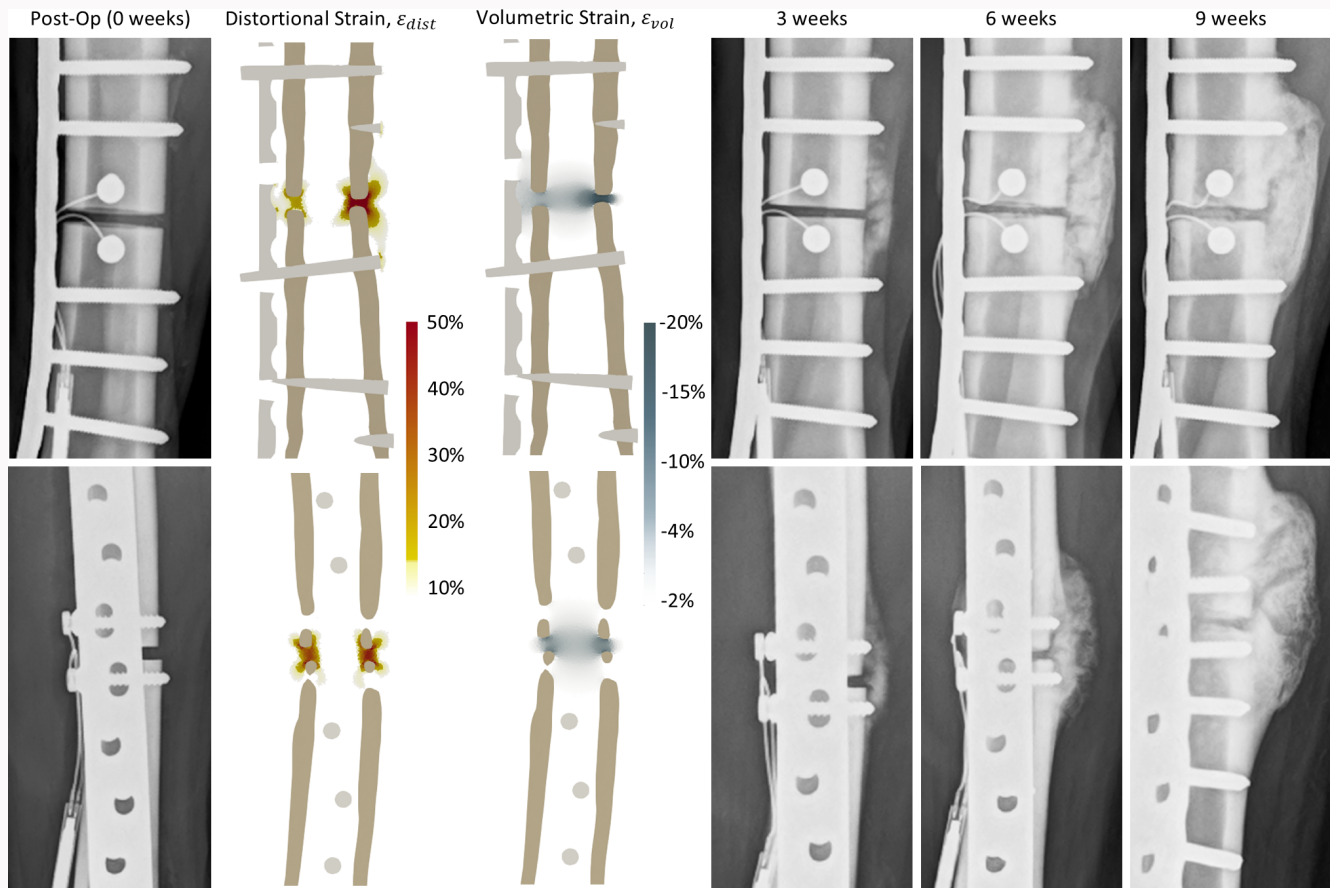
Fig. 7

Side-by-side view of distortional and volumetric strain contours with anteroposterior (top row) and mediolateral (bottom row) radiographs, which show that callus mineralization initiates outside the high-strain perifragmentary zone.

gap-closing strain before healing was above 40% and these conditions did not cause nonunion. However, at the time of kill (nine weeks), there was significantly lower mineralization in the callus located directly within versus around the osteotomy gap.

Our models also highlighted the need to consider the 3D state of strain (shape change) that is generated within the granulation tissue and early soft callus. Previous computational and experimental studies have focused on methods to measure interfragmentary motion rather than strain.[11,39–42] In contrast, our approach is unique in the application of submodelling to compute continuum strains around the fracture from the bone fragment motions. Our approach revealed that the perifragmentary region was dominated by high distortional strains arising from the "squish" effect of soft-tissue deformation in and around the fracture line. Gap-closing strains do not represent this effect, and it is important to acknowledge that shear-dominated distortion of the soft tissues can occur even without gross shearing movements of the bone fragments. Other types of fracture fixation, including intramedullary (IM) nailing, produce much more torsional motion, which would lead to even higher distortional strains but is clearly well tolerated in vivo. For example, in a published ovine study with a transverse osteotomy fixed by IM nailing, up to 10° of torsion across the fracture site was measured during gait at three weeks postoperatively.[43] For a gap distance of 3 mm, this level

of rotation corresponds to up to 100% shear strain for the interfragmentary gap tissues in the plane of the gap under pure torsion conditions. In this previous study, increasing the torsional stability of the nail did lead to superior healing outcomes, but no animals experienced a nonunion. In our models, the closest continuum component for comparison to the gap-closing (Perren) strain was the compressive volumetric strain. However, the volume of tissue experiencing high strains in pure compression was very low compared to the volume of elements experiencing high distortional strain conditions.

A side-by-side comparison of immediate postoperative strain contours with the temporal evolution of callus growth from radiograph images (Figure 7) adds to the interpretation of strain as a limiter of bone healing. Mineralization of the periosteal callus is evident as early as three weeks postoperatively, but is not evident within the osteotomy or directly adjacent to it. From three to six weeks, the callus enlarges and increases in opacity. By nine weeks, the gap zone is also mineralizing, but our results confirm the visual impression of delayed callus maturity within the gap compared to around it (Figure 6b). These observations strongly support Perren's theory that the compliance of the soft callus enables fractures to tolerate initial high strains.[27] Perren further observed that the exact strain tolerance limits for callus formation were unknown.[16,25,44] Our results reinforce that the strain tolerance limits for bone formation are still unknown. Further, our findings add to the body of data that contradicts

the widespread misinterpretation of Perren's strain theory to mean that a gap strain above 10% may lead to a nonunion.

The results from this study are subject to some limitations. While our results suggest that gap-closing strains > 10% and their associated distortional and volumetric strain fields are globally tolerable for fracture healing, our analysis cannot reveal the upper limit of strain for osteogenesis. All animals in this study had the same osteotomy gap and same plate and screws. This work is also limited by the availability of quantitative mineralization data at only a single timepoint (ex vivo microCT at nine weeks) after the osteotomy gap had already begun to consolidate. At this timepoint, substantial cortical remodelling (loss of BMD) was also evident, which made reconstruction of the native postoperative cortical boundary impossible by thresholding alone. Data from animals treated with a variety of osteotomy sizes and/or different plates, together with serial CT imaging to detect the earliest formation of callus, would be needed to discover the true tolerance limit of strain for early woven bone formation. In addition, our use of simplified screw models without threads means that these models cannot be used to infer contact stresses or study damage-induced remodelling in cortical bone near screws, a process that is known to occur in tandem with callus growth.[31]

It is also important to note that our modelling assumptions related to postoperative loading were made without the benefit of in vivo gait data. Behaviour variations over time and between animals, related to both the frequency and magnitude of loading events, could not be considered in our analysis. For this reason, we analyzed only strains related to representative peak loading during level walking, not lower-load events like partial weight transfer, or higher-load events like standing up from recumbency. Our focus on these simplified instantaneous loads is consistent with how mechanoregulatory models of fracture healing consider loading events.[45–49] However, this approach cannot account for the relative importance of high and low loading events as the physiological mechanical stimulation that drives in vivo bone formation. Investigations of activity as a regulator of bone healing are a high priority for future studies. To complement this, serum biomarkers could also be used to shed light on possible biological differences between animals that contribute to variations in callus formation, independent of activity variations.

In conclusion, this study suggests that ovine fracture healing tolerates a high-strain environment that is largely dominated by shear deformation of the soft-tissues immediately within and around the gap. The interfragmentary gap callus experiences a significant delay in mineralization compared to the periosteal callus, but this does not cause nonunion. High strain much greater than 10% appears to be a transient local limiter of osteogenesis, not a global inhibitor of secondary fracture repair.

Social media
Follow H. L. Dailey on X @DaileyOrthoLab

Supplementary material
Unabridged statistical testing results for spatial distribution of callus volume, density, and strain including tests of assumptions. An ARRIVE checklist is also included.

References

1. **Anani T**, **Castillo AB**. Mechanically-regulated bone repair. *Bone*. 2022;154:116223.
2. **Bahney CS**, **Zondervan RL**, **Allison P**, et al. Cellular biology of fracture healing. *J Orthop Res*. 2019;37(1):35–50.
3. **Marsell R**, **Einhorn TA**. The biology of fracture healing. *Injury*. 2011;42(6):551–555.
4. **Kenwright J**, **Gardner T**. Mechanical influences on tibial fracture healing. *Clin Orthop Relat Res*. 1998;355 Suppl:S179–90.
5. **Carter DR**, **Blenman PR**, **Beaupré GS**. Correlations between mechanical stress history and tissue differentiation in initial fracture healing. *J Orthop Res*. 1988;6(5):736–748.
6. **Goodship AE**, **Cunningham JL**, **Kenwright J**. Strain rate and timing of stimulation in mechanical modulation of fracture healing. *Clin Orthop Relat Res*. 1998;355S(355 Suppl):S105–15.
7. **Schell H**, **Epari DR**, **Kassi JP**, **Bragulla H**, **Bail HJ**, **Duda GN**. The course of bone healing is influenced by the initial shear fixation stability. *J Orthop Res*. 2005;23(5):1022–1028.
8. **Augat P**, **Burger J**, **Schorlemmer S**, **Henke T**, **Peraus M**, **Claes L**. Shear movement at the fracture site delays healing in a diaphyseal fracture model. *J Orthop Res*. 2003;21(6):1011–1017.
9. **Kaspar K**, **Schell H**, **Seebeck P**, et al. Angle stable locking reduces interfragmentary movements and promotes healing after unreamed nailing. Study of a displaced osteotomy model in sheep tibiae. *J Bone Joint Surg Am*. 2005;87-A(9):2028–2037.
10. **Epari DR**, **Kassi J-P**, **Schell H**, **Duda GN**. Timely fracture-healing requires optimization of axial fixation stability. *J Bone Joint Surg Am*. 2007;89-A(7):1575–1585.
11. **Elkins J**, **Marsh JL**, **Lujan T**, et al. Motion predicts clinical callus formation: construct-specific finite element analysis of supracondylar femoral fractures. *J Bone Joint Surg Am*. 2016;98-A(4):276–284.
12. **Bottlang M**, **Lesser M**, **Koerber J**, et al. Far cortical locking can improve healing of fractures stabilized with locking plates. *J Bone Joint Surg Am*. 2010;92-A(7):1652–1660.
13. **Dailey HL**, **Schwarzenberg P**, **Webb Iii EB**, **Boran SAM**, **Guerin S**, **Harty JA**. Pilot study of micromotion nailing for mechanical stimulation of tibial fracture healing. *Bone Jt Open*. 2021;2(10):825–833.
14. **Barcik J**, **Ernst M**, **Buchholz T**, et al. The absence of immediate stimulation delays bone healing. *Bone*. 2023;175:116834.
15. **Perren SM**. Physical and biological aspects of fracture healing with special reference to internal fixation. *Clin Orthop Relat Res*. 1979;138:175–196.
16. **Perren SM**. Evolution of the internal fixation of long bone fractures. The scientific basis of biological internal fixation: choosing a new balance between stability and biology. *J Bone Joint Surg Br*. 2002;84-B(8):1093–1110.
17. **Gueorguiev-Rüegg B**, **Stoddart M**. Biology and biomechanics in bone healing. In: Buckley RE, Moran CG, Apivatthakakul T, eds. *AO Principles of Fracture Management*. Third ed. Stuttgart: Georg Thieme Verlag, 2018: 9–25.
18. **Lowe JA**, **Dailey HL**, **Wild J**. Biomechanics of Internal Fracture Fixation. In: Mullis BH, Gaski GE, eds. *Synopsis of Orthopaedic Trauma Management*. First edition. Stuttgart: Georg Thieme Verlag, 2020: 24–32.
19. **No authors listed**. Fracture Healing - Basic Science. OrthoBullets. 2023. https://www.orthobullets.com/basic-science/9009/fracture-healing (date last accessed 3 December 2024).
20. **Ebraheim N**. Fracture Healing - Everything You Need To Know - Dr. Nabil Ebraheim. 2017. https://www.youtube.com/watch?v=Ovbqx5Uwmic (date last accessed 3 December 2024).
21. **The Young Orthopod**. Fracture Healing | ANIMATION | BASICS | The Young Orthopod. 2018. https://www.youtube.com/watch?v=ktWiW6yssbU (date last accessed 3 December 2024).

Don't mind the gap: reframing the Perren strain rule for fracture healing using insights from virtual mechanical testing
M. Tanveer, K. Klein, B. von Rechenberg, S. Darwiche, H. L. Dailey

13

22. **Claes L**, **Augat P**, **Suger G**, **Wilke HJ**. Influence of size and stability of the osteotomy gap on the success of fracture healing. *J Orthop Res*. 1997;15(4):577–584.

23. **Claes LE**, **Wilke HJ**, **Augat P**, **Rübenacker S**, **Margevicius KJ**. Effect of dynamization on gap healing of diaphyseal fractures under external fixation. *Clin Biomech (Bristol, Avon)*. 1995;10(5):227–234.

24. **Kenwright J**, **Goodship AE**. Controlled mechanical stimulation in the treatment of tibial fractures. *Clin Orthop Relat Res*. 1989;241:36–47.

25. **Hente RW**, **Perren SM**. Tissue deformation controlling fracture healing. *J Biomech*. 2021;125:110576.

26. **Inacio JV**, **Schwarzenberg P**, **Kantzos A**, **Malige A**, **Nwachuku CO**, **Dailey HL**. Rethinking the 10% strain rule in fracture healing: a distal femur fracture case series. *J Orthop Res*. 2023;41(5):1049–1059.

27. **Perren SM**. Fracture healing: fracture healing understood as the result of a fascinating cascade of physical and biological interactions. Part II. *Acta Chir Orthop Traumatol Cech*. 2015;82(1):13–21.

28. **Darwiche SE**, **Kaczmarek A**, **Schwarzenberg P**, **et al**. Combined electric and magnetic field therapy for bone repair and regeneration: an investigation in a 3-mm and an augmented 17-mm tibia osteotomy model in sheep. *J Orthop Surg Res*. 2023;18(1):454.

29. **Schwarzenberg P**, **Klein K**, **Ferguson SJ**, **von Rechenberg B**, **Darwiche S**, **Dailey HL**. Virtual mechanical tests out-perform morphometric measures for assessment of mechanical stability of fracture healing in vivo. *J Orthop Res*. 2021;39(4):727–738.

30. **Anup A**, **Dieterich S**, **Oreffo ROC**, **et al**. Embracing ethical research: implementing the 3R principles into fracture healing research for sustainable scientific progress. *J Orthop Res*. 2024;42(3):568–577.

31. **Ariyanfar A**, **Klein K**, **von Rechenberg B**, **Darwiche S**, **Dailey HL**. Adaptive image segmentation reveals substantial cortical bone remodeling during early fracture repair. *Comput Methods Biomech Biomed Eng Imaging Vis*. 2024;12(1):2345165.

32. **Ren T**, **Klein K**, **von Rechenberg B**, **Darwiche S**, **Dailey HL**. Image-based radiodensity profilometry measures early remodeling at the bone-callus interface in sheep. *Biomech Model Mechanobiol*. 2022;21(2):615–626.

33. **Inzana JA**, **Varga P**, **Windolf M**. Implicit modeling of screw threads for efficient finite element analysis of complex bone-implant systems. *J Biomech*. 2016;49(9):1836–1844.

34. **MacLeod AR**, **Pankaj P**, **Simpson AHRW**. Does screw-bone interface modelling matter in finite element analyses? *J Biomech*. 2012;45(9):1712–1716.

35. **Mischler D**, **Gueorguiev B**, **Windolf M**, **Varga P**. On the importance of accurate elasto-plastic material properties in simulating plate osteosynthesis failure. *Front Bioeng Biotechnol*. 2023;11:1268787.

36. **Grasa J**, **Gómez-Benito MJ**, **González-Torres LA**, **Asiaín D**, **Quero F**, **García-Aznar JM**. Monitoring in vivo load transmission through an external fixator. *Ann Biomed Eng*. 2010;38(3):605–612.

37. **Ren T**, **Dailey HL**. Mechanoregulation modeling of bone healing in realistic fracture geometries. *Biomech Model Mechanobiol*. 2020;19(6):2307–2322.

38. **Kenwright J**, **Richardson JB**, **Cunningham JL**, **et al**. Axial movement and tibial fractures. A controlled randomised trial of treatment. *J Bone Joint Surg Br*. 1991;73-B(4):654–659.

39. **Henschel J**, **Tsai S**, **Fitzpatrick DC**, **Marsh JL**, **Madey SM**, **Bottlang M**. Comparison of 4 methods for dynamization of locking plates: differences in the amount and type of fracture motion. *J Orthop Trauma*. 2017;31(10):531–537.

40. **Märdian S**, **Schaser K-D**, **Duda GN**, **Heyland M**. Working length of locking plates determines interfragmentary movement in distal femur fractures under physiological loading. *Clin Biomech (Bristol, Avon)*. 2015;30(4):391–396.

41. **Augat P**, **Penzkofer R**, **Nolte A**, **et al**. Interfragmentary movement in diaphyseal tibia fractures fixed with locked intramedullary nails. *J Orthop Trauma*. 2008;22(1):30–36.

42. **Crutcher WL**, **Magnusson EA**, **Griffith KM**, **et al**. Bridge plate fixation of distal femur fractures: defining deficient radiographic callus formation and its associations. *J Orthop Trauma*. 2023;37(10):475–479.

43. **Kaspar K**, **Schell H**, **Seebeck P**, **et al**. Angle stable locking reduces interfragmentary movements and promotes healing after unreamed nailing. study of a displaced osteotomy model in sheep tibiae. *Br J Surg Am*. 2005;87(9):2028–2037.

44. **Perren SM**. Fracture healing: fracture healing understood as the result of a fascinating cascade of physical and biological interactions. Part I. An Attempt to Integrate Observations from 30 Years AO Research. *Acta Chir Orthop Traumatol Cech*. 2014;81(6):355–364.

45. **Schwarzenberg P**, **Ren T**, **Klein K**, **von Rechenberg B**, **Darwiche S**, **Dailey HL**. Domain-independent simulation of physiologically relevant callus shape in mechanoregulated models of fracture healing. *J Biomech*. 2021;118:110300.

46. **Pietsch M**, **Niemeyer F**, **Simon U**, **Ignatius A**, **Urban K**. Modelling the fracture-healing process as a moving-interface problem using an interface-capturing approach. *Comput Methods Biomech Biomed Engin*. 2018;21(8):512–520.

47. **Wilson CJ**, **Schuetz MA**, **Epari DR**. Effects of strain artefacts arising from a pre-defined callus domain in models of bone healing mechanobiology. *Biomech Model Mechanobiol*. 2015;14(5):1129–1141.

48. **Ghiasi MS**, **Chen JE**, **Rodriguez EK**, **Vaziri A**, **Nazarian A**. Computational modeling of human bone fracture healing affected by different conditions of initial healing stage. *BMC Musculoskelet Disord*. 2019;20(1):562.

49. **Simon U**, **Augat P**, **Utz M**, **Claes L**. A numerical model of the fracture healing process that describes tissue development and revascularisation. *Comput Methods Biomech Biomed Engin*. 2011;14(1):79–93.

Author information

M. Tanveer, MS, Graduate Research Assistant
H. L. Dailey, PhD, Associate Professor
Department of Mechanical Engineering & Mechanics, Lehigh University, Bethlehem, Pennsylvania, USA.

K. Klein, DVM-PhD, Co-Director
S. Darwiche, PhD, Co-Director
Musculoskeletal Research Unit (MSRU), Vetsuisse Faculty, University of Zurich, Zurich, Switzerland.

B. von Rechenberg, DVM, Founder and Emeritus Head, Co-Founder, Musculoskeletal Research Unit (MSRU), Vetsuisse Faculty, University of Zurich, Zurich, Switzerland; Competence Center of Applied Biotechnology and Molecular Medicine (CABMM), Vetsuisse Faculty, University of Zurich, Zurich, Switzerland.

Don't mind the gap: reframing the Perren strain rule for fracture healing using insights from virtual mechanical testing
M. Tanveer, K. Klein, B. von Rechenberg, S. Darwiche, H. L. Dailey

15